Nanoscale

PAPER

View Article Online
View Journal

Cite this: DOI: 10.1039/c7nr02672b

Spatially distinct Raman scattering characteristics of individual ZnO nanorods under controlled polarization: intense end scattering from forbidden modes†

Matthew Hansen, Johnson Truong, Tian Xie and Jong-in Hahm *

In this study, we characterize incident/scattered polarization-specific and NR position-resolved Raman scattering behaviors of individual zinc oxide nanorods (ZnO NRs). We quantify Raman signals from the five key ZnO phonon modes of E_{2L}, E_{2H-2L}, A_{1T}, E_{1T}, and E_{2H}, and reveal the NR position-dependent Raman scattering characteristics of the phonon modes per given light–matter interaction geometry. We then present Raman intensity maps and elucidate Raman behaviors consistent and incongruous with Raman selection rules. In particular, we identify an intriguing Raman scattering phenomenon from the forbidden modes, distinctively occurring at the two NR ends. Their unexpectedly strong and localized scattering signals at the NR termini are contrasted by the scattering behaviors from the rest of the NR positions agreeing with the selection predictions. By carrying out control measurements on isotropic ZnO microparticles (MPs), we ascertain that the unique NR position-specific Raman responses observed on ZnO NRs originate from their high shape anisotropy. Owing to the superior optical property coupled with reduced dimensionality and high geometric anisotropy, ZnO NRs have gained much attention recently for use in optoelectronic, photonic, and biosensor technologies. Raman scattering has been increasingly exploited as a noninvasive and sensitive analytical tool to investigate NR properties pertinent to these applications. Hence, our endeavors, explicitly providing the spatially distinct, polarized Raman scattering behaviors from individual ZnO NRs, will be central to the correct interpretation of Raman data of both the individual and ensemble NRs as well as to the accurate correlation of the measurement outcomes to their chemical/physical/optical properties. Our efforts may also promote novel applications for polarized Raman scattering whose optical outputs on the various positions along the ZnO NRs can be selectively modulated.

Received 14th April 2017,
Accepted 5th June 2017

DOI: 10.1039/c7nr02672b

rsc.li/nanoscale

Introduction

Nanoscale zinc oxide (ZnO) materials exhibit useful optical properties which have facilitated their applications in photoconduction, waveguiding, light collection, light emission, lasing, optical routing, and biosensing.[1–5] In particular, one-dimensional (1D) ZnO materials in the form of nanowires (NWs) and nanorods (NRs) have been proven effective in previous studies for optical applications geared towards operation in a highly miniaturized format.[2,3,6,11] Recent endeavors in ZnO NR-based elastic/inelastic scattering,[12–15] active/passive light guiding[2,3,6–8,16–20] and lasing[2,9–11,21,22] have utilized the employment of single NRs instead of their bulk counterparts or NR ensembles. Central to such functional use of 1D ZnO NRs is the precise understanding of the light–matter interaction between individual ZnO NRs and incident (excitation) as well as the scattered (emitted/guided) light. The light–matter interaction characteristics have been carefully scrutinized in the past[13,15] for the elastic scattering behaviors of ZnO NRs as well as for the subwavelength waveguiding of fluorescence signals coupled into ZnO NRs from nearby fluorophores.[18–20,23] In both of these cases, the high shape anisotropy inherent to 1D ZnO NRs was shown to have significant effects on the magnitude and direction of the optical signals measured from discrete ZnO NRs, demonstrating the importance of the light–matter interaction geometry not only for the

Department of Chemistry, Georgetown University, 37th & O Sts. NW., Washington, DC 20057, USA. E-mail: jh583@georgetown.edu

†Electronic supplementary information (ESI) available: More representative Raman spectra are presented in Fig. S1. They are the ensemble-averaged Raman data from a sample containing as-synthesized ZnO NRs and the position-specific Raman spectra from a vertically oriented ZnO NR. Additional material characterization data of ZnO NRs are provided in Fig. S2. They are the X-ray diffraction data, PL spectra upon excitation above the ZnO bandgap, emission spectra as well as image upon excitation below the bandgap. See DOI: 10.1039/c7nr02672b

effective manipulation of incident light but also for the optical outcomes of NR-originated and NR-guided signals. However, very few studies are currently available for systematic light–matter examinations pertinent to Raman scattering of individual ZnO NRs.

Raman scattering has been employed for identifying the chemical composition, defect state, lattice dynamics, and phonon confinement of various materials. More recently, Raman spectroscopy has been demonstrated as a convenient and nondestructive analytical tool for obtaining information on ZnO nanostructures such as the growth direction, morphology, structure, crystalline lattice order, and self-assembly process.[24–29] For example, a shift in E_2 high peak from the bulk ZnO value[24–26] of 437–439 cm^{-1} can be an indication of internal stress present in the crystalline lattice of ZnO.[27,28] The intensities of A_1 transverse optical and E_2 high modes can be linked to provide information on the ZnO NR diameter.[27] However, the characteristic Raman spectra of ZnO nanomaterials can be strongly governed by the aforementioned light–matter interaction geometry, especially for ZnO NRs with high shape anisotropy. Therefore, elucidation of the exact nature and consequence of the light–matter interaction related to Raman scattering phenomenon of individual ZnO NRs is important in accurately and meaningfully relating the Raman measurement outcomes in peak intensities and shifts to the nanomaterial characteristics. To date, only few studies have examined polarization-resolved Raman scattering behaviors of individual ZnO NRs.[28,30,31] There still exits a lack of systematic studies on the effects of light polarization and shape anisotropy on the Raman scattering behavior of single ZnO NRs, particularly related to spatially resolved Raman scattering characteristics along individual NRs.

In this paper, we unambiguously determine the precise effects of incident/scattered light polarization on key Raman active modes of ZnO NRs. We ascertain the varying degrees of Raman responses of specific Raman modes and their variations as a function of the position on the NRs. In addition to the dominant Raman scattering modes of wurtzite ZnO for given light–matter interaction geometry as dictated by Raman selection rules, we identify very intriguing, highly localized scattering behaviors from the forbidden modes. The Raman scattering signals corresponding to the forbidden modes are absent along the main body of the NRs while the two ends of the NRs display strikingly strong signals. By comparing the spatially resolved, polarization-controlled Raman scattering profiles of the NRs with those of MPs, we explicitly demonstrate that the origin of the uniquely observed Raman behaviors at the NR ends is attributed to the high shape anisotropy of the nanomaterial.

Experimental details

ZnO NRs and MPs were synthesized in a home-built, chemical vapor deposition reactor, similar to the previously described procedures.[9,32–35] Using 20 nm Au colloids (Ted Pella, Inc.; Redding, CA.) as catalysts, subsequent ZnO growths were carried out on a Si growth substrate (Silicon Quest International Inc., San Jose, CA). The source materials obtained from Alfa Aesar Inc., 0.45 grams of a 2 : 1 mixture of graphite (99%) to zinc oxide powders (99.999%), were placed in a quartz boat at the center of a horizontal resistance furnace and a target boat containing the catalyst-deposited Si substrate was placed at approximately 15 cm downstream. The furnace was then heated to 850–950 °C for 15–35 min at a ramp up/ramp down rate of 15 °C min^{-1} under a constant Ar flow of 100 standard cubic centimeters per minute. As-synthesized ZnO NRs were sonicated off from the growth substrate and dispersed in ethanol. A drop-wise deposition of the ZnO NRs in ethanol onto a clean Si wafer led to NRs lying flat on the Si surface. ZnO MPs were used as-prepared directly after their growth. For morphological characterization of the ZnO NRs and MPs, the samples were imaged using a FEI/Philips XL 20 scanning electron microscope (SEM) operating at 20 kV.

Raman spectra were collected using a LabRAM HR Evolution Raman confocal microscope (Horiba Instruments Inc., Sunnyvale, CA) with a 100× objective lens of a numerical aperture value of 0.9 (Olympus Corp., Waltham, MA). A linearly polarized 532 nm laser with a power setting of 25 mW was used to illuminate individual ZnO NRs (MPs) as a function of position along the NR (MP) on a computer-controlled motorized XY stage. For 2D mapping of Raman signals, the DuoScan option of fast mapping was employed under which the laser was scanned over individual NRs held at fixed positions on the sample stage. In a typical Raman mapping run, the laser beam of approximately 1 μm in diameter was rastered over a ZnO NR area of interest in steps ranging 550–750 nm and 270–440 nm along the long and short axis of the NR, respectively. Subsequently, the position-resolved Raman data from individual ZnO NRs and MPs of different orientations were collected in the scan range of 50–500 cm^{-1} using a 1800 lines per mm grating and a charge-coupled-device (CCD) detector. For direction-controlled collection of Raman scattered signals from the samples, a second polarizer referred to as an analyzer was placed prior to the spectrophotometer and detector. For producing unpolarized measurement conditions, a scrambler, a $\lambda/4$ waveplate, was inserted in the beam path in the absence of the analyzer.

Results and discussion

A schematic representation of the measurement setup to examine the Raman scattering behaviors of individual ZnO NRs as a function of incident/scattered light polarization and position along the NR is given in Fig. 1A. The illumination source is a 532 nm diode-pumped solid state laser that is linearly polarized with the polarization ratio greater than 100 : 1 in the z-direction, as designated by the blue double arrow and labelled as E_{inc} in Fig. 1A. The light entering through the objective lens of the confocal microscope illuminates the ZnO NR sample from above (x-direction). The scattered light is then

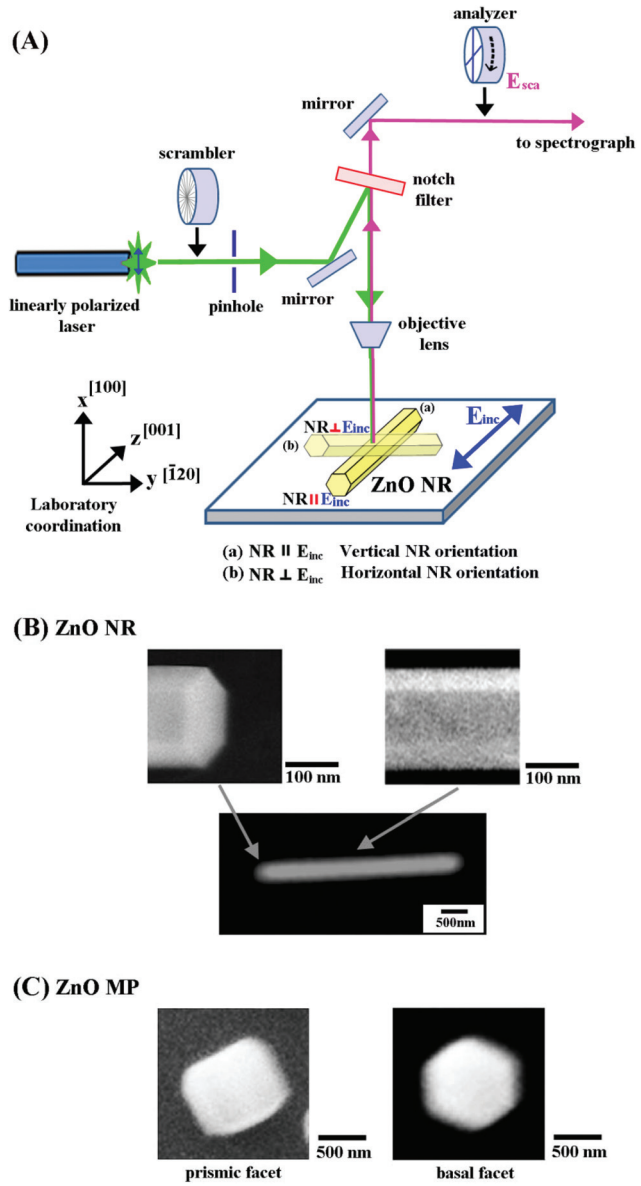

Fig. 1 (A) A schematic illustration displaying the overall measurement setup for Raman scattering of individual ZnO NRs with well-defined orientations on a Si wafer. The orientation of the *c*-axis of the wurtzite ZnO NR crystal is controlled vertical (or horizontal), producing a measurement condition which the long axis of the NR is parallel (or perpendicular) to the laser polarization. When needed, a scrambler or an analyzer is placed in the beam path to yield either conditions for unpolarized illumination or cross polarized detection, respectively. The laboratory coordinate displays the crystalline facet directions of a vertically placed ZnO NR with respect to the *x*, *y*, and *z* axes. (B) SEM images of a representative ZnO NR used in our Raman measurements showing the crystal's hexagonal end and rectangular side (main body) facets. (C) Typical SEM images of ZnO MPs used in control experiments.

collected in a backscattering configuration where it passes through to the spectrograph. For the experiments conducted under an unpolarized setting, a $\lambda/4$ plate (designated as scrambler in Fig. 1A) can be inserted between the illumination source and the pinhole. Likewise, for experiments requiring control over the polarization state of the scattered light, an analyzer can be placed prior to the spectrograph. In lieu of altering the polarization of the laser in these experiments, we measured two sample conformations the ZnO NRs, vertical and horizontal. This detection configuration ensures that no potential variations in the polarization-dependent optical constants associated with different optical components in the setup will affect the measurement outcomes. Vertical NRs correspond to NRs oriented with their long axis (*c*-axis) parallel to the direction of polarization ($NR \| E_{inc}$), whereas horizontal NRs have their long axis oriented perpendicular to the incident polarization ($NR \perp E_{inc}$). The three-axis diagram shown next to the sample plane in Fig. 1A displays the crystalline facet directions of a vertically placed ZnO NR with respect to the laboratory coordinates of *x*, *y*, and *z*. NR position-specific Raman scattering signals can be obtained by focusing the laser beam of approximately 1 μm in diameter on different NR locations. For NR spectra presented with no specific indication of the laser beam position on the NRs, the illumination was centered on the middle part of the NRs, as the schematic depicts in Fig. 1A.

Fig. 1B shows representative SEM images of wurzite-type ZnO NRs used in this experiment. The exterior surfaces of wurzite ZnO NRs show two main crystalline facets; the basal facet (the hexagonal planes found at the two NR ends) and the prismic facet (the rectangular planes found along the NR main body). The SEM images also show that the NR crystalline facets are catalyst particle-free after undergoing the steps to redisperse ZnO NRs onto a clean Si substrate after their synthesis. The NRs examined in this study exhibit aspect ratios in width : length of 1 : 15–1 : 75, typically ranging from a few hundred nanometers in width and several to ten of micrometers in length. In contrast, the images in Fig. 1C are typical SEM images of the ZnO MPs which were used as a control to study the effect of the nanomaterial's shape anisotropy on Raman scattering. The hexagonal (basal) and rectangular (prismic) facets are also clearly seen in the SEM images of the ZnO MPs, typically exhibiting an aspect ratio of ~1 : 1.

Wurtzite ZnO, belonging to the space group of C^4_{6v}, has the optical modes of $\Gamma_{opt} = A_1 + 2B_1 + E_1 + 2E_2$ at the Γ point of the Brillouin zone according to group theory.[25,36–38] A_1 and E_1 are Raman active whose polar modes split into different frequencies for the transverse-optical (TO) and longitudinal-optical (LO) modes. The nonpolar E_2 mode is also Raman-active and its symmetry allows two frequencies of high and low E_2, *i.e.* E_{2H} and E_{2L}, respectively. The E_{2H} mode is associated with oxygen atoms whereas E_{2L} is related to Zn atoms. B_1 is Raman-silent.

Fig. 2A shows a typical Raman spectrum taken from single ZnO NRs in the scan range of 75–500 cm^{-1}. The five peaks of interests (labelled i–v) appear at 98, 331, 378, 413, and 437 cm^{-1} for the NRs and they correspond to the E_{2L}, E_{2H-2L}, A_{1T}, E_{1T}, and E_{2H} mode, respectively. The Raman spectra taken from dense ZnO NRs as-synthesized on the Si growth wafer are provided in ESI, Fig. S1(A).† Unlike all five modes resolved in

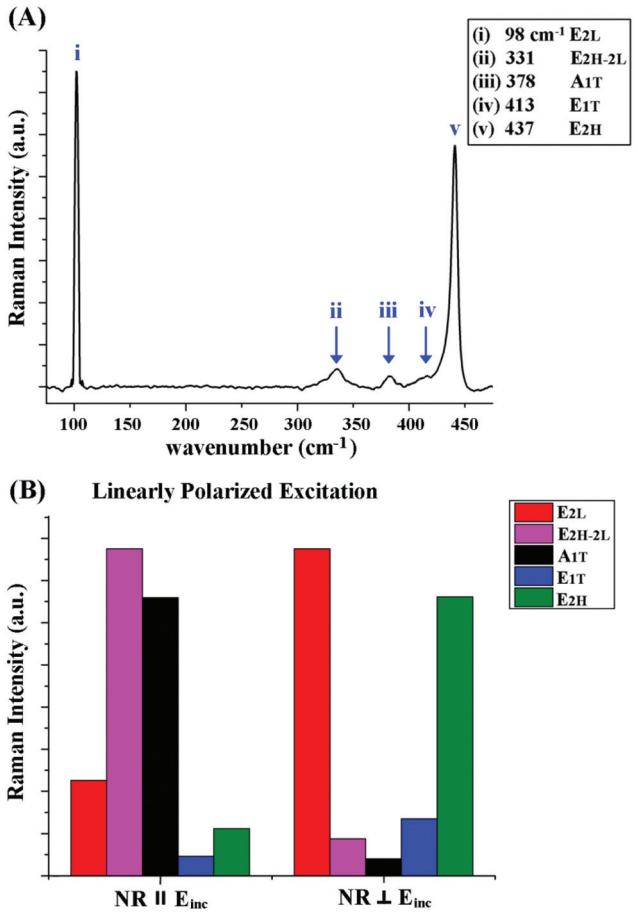

Fig. 2 Raman spectra were collected from ZnO NRs using a linearly polarized laser. All scattered signals from the NRs were collected regardless of their polarization states. (A) A typical Raman spectrum taken from a ZnO NR is shown in the fingerprint wavenumber region of 75–500 cm^{-1}. The peaks of focus in this study correspond to the (i) E_{2L} mode at 98 cm^{-1}, (ii) E_{2H}–E_{2L} mode at 331 cm^{-1}, (iii) A_{1T} mode at 378 cm^{-1}, (iv) E_{1T} mode at 413 cm^{-1}, and (v) E_{2H} mode at 437 cm^{-1}. (B) Polarization-dependent Raman scattering behaviors of ZnO NRs were examined from a large number of individual ZnO NRs while sampling random positions on the NRs. Averaged intensities at the five peaks were normalized with respect to the highest intensity mode and subsequently graphed for the two different NR orientations, parallel and perpendicular to the incident polarization. When ZnO NRs were in parallel direction to the laser polarization, the prominent Raman intensities collected were the E_{2H}–E_{2L} and A_{1T} modes. The E_{2L} and E_{2H} peaks were largely suppressed. On the contrary, ZnO NRs oriented perpendicular to the laser polarization yielded extremely strong Raman intensities from the E_{2L} and E_{2H} modes relative to the other modes. The E_{1T} mode was weak under both orientations.

the Raman spectra of individual NRs in Fig. 2(A), the Raman spectrum of as-synthesized NR samples showed E_{2L}, E_{2H-2L}, E_{1T}, and E_{2H} peaks but not A_{1T}, similar to the previously reported cases of ZnO thin films.[39,40] According to Raman selection rules, the five peaks of individual ZnO NRs will tend to emerge or disappear depending on the orientation of the NR with respect to the polarization of the incident light (E_{inc}) and that of the scattered light (E_{sca}). We first focus on measurement conditions in the absence of the analyzer and reserve our discussion for cross-polarized conditions for later in this paper.

Fig. 2B shows the scattering intensity of each of the 5 peaks discussed above for both the NR$\|E_{inc}$ and NR$\perp E_{inc}$ cases averaged from 30 ZnO NRs. Raman scattering profiles from arbitrary positions on the NRs were examined in this analysis, sampling 30 spots and 67 spots from the NR$\|E_{inc}$ and the NR$\perp E_{inc}$ configuration, respectively. The apparent differences in the dominant Raman modes for the two cases are clearly seen when comparing the average Raman intensities taken from the five peaks. For the NR$\|E_{inc}$ orientation, the relative intensity ratios of the five peaks are 0.3 : 1 : 0.85 : 0.06 : 0.14 (E_{2L} : E_{2H-2L} : A_{1T} : E_{1T} : E_{2H}). Therefore, for the vertically positioned ZnO NRs, the E_{2H-2L} and A_{1T} peaks are the predominant features and the remaining peaks are much weaker in intensity. For the NR$\perp E_{inc}$ orientation, the relative Raman intensities between the five peaks change to 1 : 0.1 : 0.05 : 0.17 : 0.85 (E_{2L} : E_{2H-2L} : A_{1T} : E_{1T} : E_{2H}). Hence, the predominant features for the horizontal ZnO NRs are the E_{2L} and E_{2H} peaks, while the remaining three peaks are weak. The relative intensity contribution from the E_{1T} mode is small in both cases.

Under the measurement condition involving polarization control over the incident light only (*i.e.* with no analyzer) in a backscattering geometry, the Raman selection rules suggest particular sets of Raman processes for the five peaks under investigation.[30,31,36] They are detailed in Table 1 for the vertically and horizontally oriented ZnO NRs when all polarization states of the scattered light are collected.

We subsequently compared the Raman intensities of the allowed modes for each light–matter interaction geometry. The A_{1T} peak at 378 cm^{-1}, allowed both for NR$\|E_{inc}$ and NR$\perp E_{inc}$ according to Table 1, was present for both vertical and horizontal cases in Fig. 2B where its intensity was strong (extremely weak) for vertical (horizontal) ZnO NRs. The signals corresponding to the E_{2L} (98 cm^{-1}) and E_{2H} (437 cm^{-1}) modes, allowed only for NR$\perp E_{inc}$ in Table 1, appeared weak for the vertical ZnO NRs in Fig. 2B, whereas they were the dominant intensity peaks for the horizontal NRs. Therefore, upon analyzing Raman data taken from arbitrarily chosen NR positions averaged over many ZnO NRs, our experimental observations

Table 1 Raman modes allowed for the vertically and horizontally placed ZnO NRs under the backscattering configuration with the polarization control of the incident light

NR orientation	Frequency	Process	Observation geometry using the porto notation
Vertical NRs	378 cm^{-1}	A_{1T}	$x(zz)\bar{x}$
	413 cm^{-1}	E_{1T}	$x(zy)\bar{x}$
	331 cm^{-1}	E_{2H}–E_{2L}	$x(zz)\bar{x}$
Horizontal NRs	378 cm^{-1}	A_{1T}	$x(yy)\bar{x}$
	413 cm^{-1}	E_{1T}	$x(yz)\bar{x}$
	437 cm^{-1}	E_{2H}	$x(yy)\bar{x}$
	98 cm^{-1}	E_{2L}	$x(yy)\bar{x}$

agree well with the Raman selection rules for the predicted allowed modes and concur with the previously reported trend of dominant A_1 with weak E_2 signals under NR$\|E_{inc}$ as supposed to the very strong E_2 with minor A_1 intensities under NR$\perp E_{inc}$. Between the two light–matter interaction geometry, the Raman intensity ratio of A_{1T} between the cases of NR$\|E_{inc}$ and NR$\perp E_{inc}$ is ~1 : 3. The intensities of the E_{2L} and E_{2H} peaks between NR$\|E_{inc}$ and NR$\perp E_{inc}$ are ~21 : 1 and 36 : 1, respectively. The large difference and, hence, the high sensitivity to the incoming polarization shown for the E_2 symmetry relative to A_1 is likely because E_2 is allowed only for NR$\perp E_{inc}$, unlike A_1 permitted for the parallel and perpendicular geometries. In addition, we clearly observe the E_{2H}–E_{2L} peak at 331 cm^{-1} which is associated with a 2nd order multiphonon scattering. The much more pronounced E_{2H}–E_{2L} signal for the vertical than horizontal NRs is also in agreement with previously reported results.[36]

In order to understand the exact consequence of light interaction as a function of light polarization state and position along the NR, the data summarized in Fig. 3 display the incident polarization-specific Raman scattering outcomes measured from the middle position of a single ZnO NR. Fig. 3 (A) and (B) show the effect of using linearly polarized *versus* unpolarized light as an illumination source when probing the same ZnO NR oriented either vertically or horizontally. The polarized scattering results from the NR$\|E_{inc}$ and NR$\perp E_{inc}$ cases are then combinedly shown in Fig. 3A for comparison. Similar to what was observed in the NR- and position-averaged spectra in Fig. 2B, the single NR yielded the same predominant E_{2H} and E_{2L} peaks under NR$\perp E_{inc}$ while the A_{1T} and E_{2H-2L} peaks were the strongest in the NR$\|E_{inc}$ orientation. The relative intensity ratios of the $E_{2L} : E_{2H-2L} : A_{1T} : E_{1T} : E_{2H}$ peaks under NR$\|E_{inc}$ and NR$\perp E_{inc}$ were also similar to the values discussed for Fig. 2.

The effect of unpolarized incident light on the Raman spectra of the same ZnO NR in Fig. 3A is displayed in Fig. 3B. The scattering intensity differences of the five peaks between the NR$\|E_{inc}$ and NR$\perp E_{inc}$ cases have significantly reduced under the unpolarized illumination relative to the linearly polarized case. The E_{2L} and E_{2H} peaks appeared strong even for the vertical orientation under unpolarized light, which was not the case under the polarized light. This indicates that the relative contributions from the minor modes in the vertical *versus* horizontal orientations (E_{2L} and E_{2H} *versus* E_{2H}–E_{2L} and A_{1T}, respectively) have increased greatly under the unpolarized illumination. At the same time, the signal contributions from E_{1T}, which produced relatively minor peaks in both orientations under the linearly polarized light, have also risen considerably under no polarization.

The reported NR Raman behaviors in this paper are not related to potential heating or mechanical damage at the NR ends induced by the focused laser. The laser output power of 25 mW used in our experiments is comparable to the typical Raman measurement conditions, often involving a power setting up to 500 mW. Also, in subwavelength waveguiding, UV lasing, and UV photoluminescence studies, ZnO NRs are known to be stable even after prolonged exposure to a short pulsed, high power laser that can reach a peak power well above 10^5 W.[6,8,10,17]

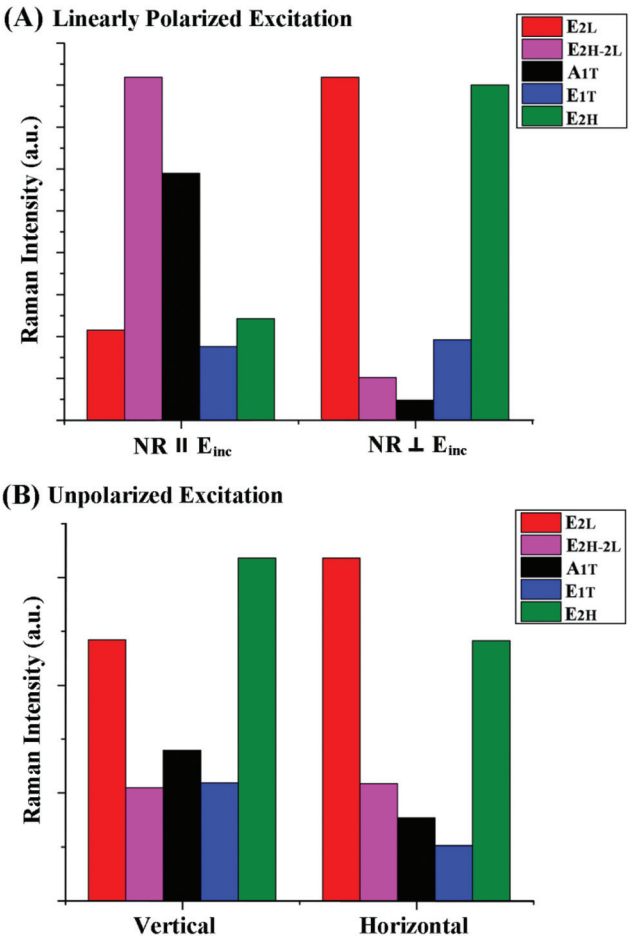

Fig. 3 Raman scattering behaviors of single ZnO NRs were systematically investigated by examining the effect of polarized *versus* unpolarized light on the scattering profiles of the same ZnO NR while varying its orientation. The incident beam was centered in the middle of the NR and all scattering signals were collected regardless of the polarization state of the scattered light. Normalized Raman intensities with respect to the highest intensity peak are then plotted for the five phonon modes. (A) The bar graphs show the principal modes as well as the relative intensity ratios between the five peaks for both the NR$\|E_{inc}$ *versus* NR$\perp E_{inc}$ orientations. For each NR orientation, polarization-dependent Raman spectra resulted in consistent trends in the intensity ratios between the five modes as discussed in Fig. 2. (B) When unpolarized light was used instead for illumination on the same NR placed either vertically or horizontally, the dominant peaks remained the same as E_{2L} and E_{2H}, regardless of the NR placement.

Subsequently, Raman intensity maps of single ZnO NRs were collected by rastering the incident beam over the same NRs placed in both the NR$\|E_{inc}$ and NR$\perp E_{inc}$ orientations. Fig. 4 summarizes the rastering Raman results of the same ZnO NR discussed in Fig. 3. The spatially resolved, Raman heat maps consist of all scattered signals regardless of their polarization states. Raman maps for each of the five phonon modes of the ZnO NR were then generated. The 3D contour

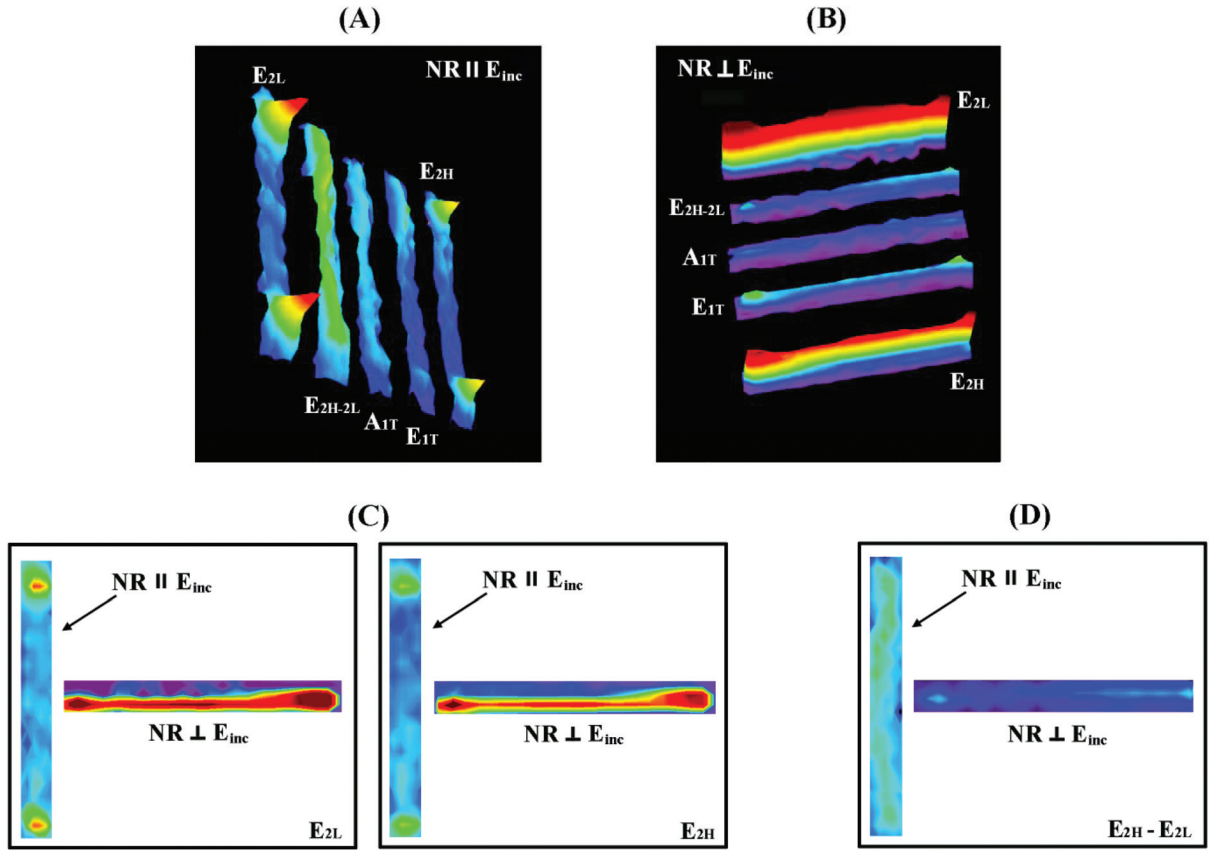

Fig. 4 Raman intensity maps of the five ZnO phonon modes are displayed combinedly for the different light–matter interaction geometries. The data show strongly NR position-dependent Raman scattering profiles for the minor modes per given orientation, whereas the major modes for each orientation display continuous and persistent Raman intensities distributed all along the entire NR length. (A and B) 3D contour profiles of the Raman intensities were mapped for the five peaks under (A) NR$\|E_{inc}$ and (B) NR$\perp E_{inc}$. The NR end-related scattering behaviors of the minor modes can be seen from the E_{2L} and E_{2H} slices in (A) and from the $E_{2H}-E_{2L}$ and A_{1T} slices in (B). (C and D) For clarity, the 2D surface maps for the same ZnO phonon modes taken under the two light–matter interaction geometries are displayed side by side. The Raman maps for the E_{2L} and E_{2H} modes in (C) clearly display discrete (continuous) scattering intensities at the two ends (all along the NR) when the NR is oriented parallel (perpendicular) to the laser polarization. The opposite trend is observed in (D) for the $E_{2H}-E_{2L}$ mode. The NR ends tend to produce higher scattering than other positions on the NR for $E_{2H}-E_{2L}$ under NR$\perp E_{inc}$, whereas NR$\|E_{inc}$ leads to continuous Raman signals along all positions on the NR.

plots in Fig. 4A and B show the resulting intensities for the ZnO NR oriented parallel and perpendicular to the incident polarization, respectively. The 3D slices are displayed in color gradients ranging from red (high intensity) to blue (low). Each slice in the series of Raman maps presented in Fig. 4A and B represents the scattering signals associated with the E_{2L}, E_{2H-2L}, A_{1T}, E_{1T}, and E_{2H} mode as indicated next to each map. When inspecting the slices corresponding to the major modes of E_{2H-2L} and A_{1T} in Fig. 4A, their scattering intensities were present continuously along the entirety of the NR. This trend can be seen by the green and sky blue region in the E_{2H-2L} and A_{1T} slice, respectively, spanning the whole length of the NR. A similar effect is seen in Fig. 4B for the same NR in the horizontal orientation for its major modes. Raman signals from the E_{2H} and E_{2L} were continuously observed along the entire length of the NR, as displayed in the topmost and bottommost slices in Fig. 4B.

In ensuing examination of the minor modes for each orientation, their scattering intensities were largely absent from the NR main body but appeared as highly enhanced and spatially localized signals at the two ends of the NR. For the NR$\|E_{inc}$ geometry in Fig. 4A, the signals from the E_{2H} and E_{2L} modes were suppressed along the NR main body as expected. Yet, the Raman maps for these two minor modes clearly resolve the highly intense scattering at the two NR ends. This phenomenon can be further evidenced by the NR position-specific Raman scattering data presented additionally in ESI, Fig. S1 (B).† The two spectra obtained from a vertically oriented ZnO NR (NR$\|E_{inc}$) clearly show that, in addition to the dominant modes of E_{2H-2L} and A_{1T} peaks in both the NR end and middle spectra, the forbidden modes of E_{2L} and E_{2H} peaks were detected in the NR end spectrum. In contrast, the Raman spectrum of the NR middle position of the same ZnO NR did not show any scattering from these forbidden modes. Similarly, this unusual NR end behavior was also observed from the NR$\perp E_{inc}$ orientation. In this case, the modes of E_{2H-2L} and E_{1T} with negligible scattering along the NR main body yielded noticeably high scattering intensities at the NR ends.

This intriguing Raman scattering phenomenon at NR ends can be seen more clearly in the 2D intensity profiles in Fig. 4C and D. In these heat maps, the 2D projected views of the mapped Raman data for the E_{2H}, E_{2L}, and E_{2H-2L} modes are presented side by side, comparing the different scattering behaviors from the same mode under the NR$\|E_{inc}$ *versus* NR$\perp E_{inc}$ orientations. For the same phonon mode, the continuous scattering profile along the NR, when the modes are allowed, switches to intense, NR end-confined scattering profile when the light interaction geometry changes such that these modes become forbidden. Data in Fig. 4C and D show the scattering profile of highly intense NR end and largely suppressed main body from the E_{2H} and E_{2L} modes under NR$\|E_{inc}$ and from the E_{2H-2L} mode under NR$\perp E_{inc}$. The 2D heat maps also show that, when the NR orientation with respect to the incident light is such that the given mode becomes a dominant transition, the corresponding Raman signal is continuously present along the length of the NR. This corresponds to the NR$\perp E_{inc}$ geometry for E_{2H} and E_{2L} and to the NR$\|E_{inc}$ geometry for E_{2H-2L}. In brief, our observations indicate the NR end-exclusive Raman scattering effect occurs for the minor modes per given light–matter interaction geometry. Major phonon modes exhibit NR position-independent scattering whose signal presence followed the predictions from the Raman selection rules. In contrast, minor modes produce the unexpected, NR end-related, Raman scattering characteristics. Possible origins of the NR end-related abnormalities will be discussed later, following the measurement outcomes of cross polarizer configurations.

We continued to investigate the Raman scattering behavior of individual ZnO NRs by additionally controlling the polarization state of the scattered signal (E_{sca}) and subsequently examining agreements and deviations from the Raman selection rules. We accomplished this by placing an analyzer prior to the detector and altering its angle from 0 to 90 degrees (°), while probing the middle position of the ZnO NRs. As the analyzer angle is changed from 0° and 90°, the cross polarization setting changes from $E_{inc}\|E_{sca}$ to $E_{inc}\perp E_{sca}$. These cross-polarized Raman scattering data were systematically collected for the NR orientation of NR$\|E_{inc}$ as well as for NR$\perp E_{inc}$ and changes in Raman intensities associated with the dominant phonon modes per light interaction setting were inspected. In addition, E_{1T} was included in the evaluation since the Raman selection rules suggest E_{1T} as the only allowed mode when the polarization state of E_{sca} is perpendicular to that of E_{inc}. Fig. 5A displays the different tendencies observed for the polarization states of the scattered signals corresponding to the two dominant (A_{1T} and E_{2H-2L}) and E_{1T} modes measured under NR$\|E_{inc}$. In both the scatter plot and the bar graph for E_{1T} in Fig. 5A, it can be seen that E_{1T} exhibits a very steep rise in intensity when the analyzer rotation becomes close to $E_{inc}\perp E_{sca}$. The Raman intensities belonging to the A_{1T} and E_{2H-2L} peaks either decrease or only show a slight increase for $E_{inc}\perp E_{sca}$. Fig. 5B displays the scattering intensity of the two dominant (E_{2H} and E_{2L}) as well as the E_{1T} modes under NR$\perp E_{inc}$ for the same NR. Similar to the NR$\|E_{inc}$ case, the E_{1T} intensity showed a considerable increase as the analyzer angle changed to the $E_{inc}\perp E_{sca}$ condition whereas the intensities from the E_{2H} and E_{2L} modes decreased as the analyzer rotation was changed towards $E_{inc}\perp E_{sca}$.

According to the selection rules in Table 1, the allowed Raman mode for wurzite ZnO NRs probed in the $x(zy)\bar{x}$ or $x(yz)\bar{x}$ configuration is the E_{1T} mode, and under these configurations, other modes become forbidden. Hence, our observation of higher E_{1T} intensities with increasing analyzer rotation towards $E_{inc}\perp E_{sca}$ is consistent with what is predicted for NR$\|E_{inc}$ and NR$\perp E_{inc}$. Yet, forbidden modes such as the A_1 and E_2 modes were also observed with weak intensities. The nonvanishing peaks of forbidden modes in the ZnO NR spectra may be attributed to potential deviations in the NR placement with respect to the light polarization. In ZnO, the transverse optical (TO)-longitudinal optical (LO) splitting is much larger (hundreds of cm^{-1}) than the A_1–E_1 splitting (tens of cm^{-1}). Mixing of A_l and E_l modes can occur if the phonon propagation direction is not perfectly in parallel or perpendicular to the crystal axis.[41] Therefore, slight errors in the ZnO NR alignment with respect to the polarization direction may be enough to produce this intermediate phonon propagation situation, resulting in the weak presence of the forbidden modes.

However, this does not explain the unique findings pertaining to the NR end-confined abnormalities detailed earlier. The unusual phenomena summarized in Fig. 4 differ from what were reported in previous works for explaining the non-vanishing forbidden modes.[30,31] In those studies, the weak to moderate signals of forbidden Raman bands were generally attributed to the defects such as O or Zn vacancy in the ZnO crystalline lattice as well as to the physical disorder in ZnO. Examples of the latter include non-uniform crystal growth along the *c*-axis and small grains found on the surface of ZnO nanostructures. ZnO nanostructures in these previous studies were synthesized *via* hydrothermal methods and the presence of chemical and physical defects were confirmed by photoluminescence and electron microscopy.[30,31] However, ZnO NRs in this work were synthesized *via* a gas phase approach which has shown to yield highly crystalline and atomic defect-free NR crystals.[42,43] The X-ray diffraction data and additional luminescence data of the ZnO NRs used in this study are provided in ESI, Fig. S2.† The data clearly demonstrate that the ZnO NRs are optical quality materials whose luminescence image and spectra, taken by using both the below- and above-bandgap excitation, showed no visible emissions characteristic of atomic defects. Only an intense UV photoluminescence peak associated with the ZnO bandgap appeared at 388 nm when the NRs were excited with 337 nm light.

Therefore, the same explanation for non-vanishing forbidden modes described in previous works do not apply to the polarization- and position-dependent Raman outcomes of ZnO NRs discussed here. In addition, we reveal that only forbidden modes produce the high scattering signals localized at the two NR ends. Their signals on the NR main body, on the contrary, follows the general behavior of the forbidden modes as

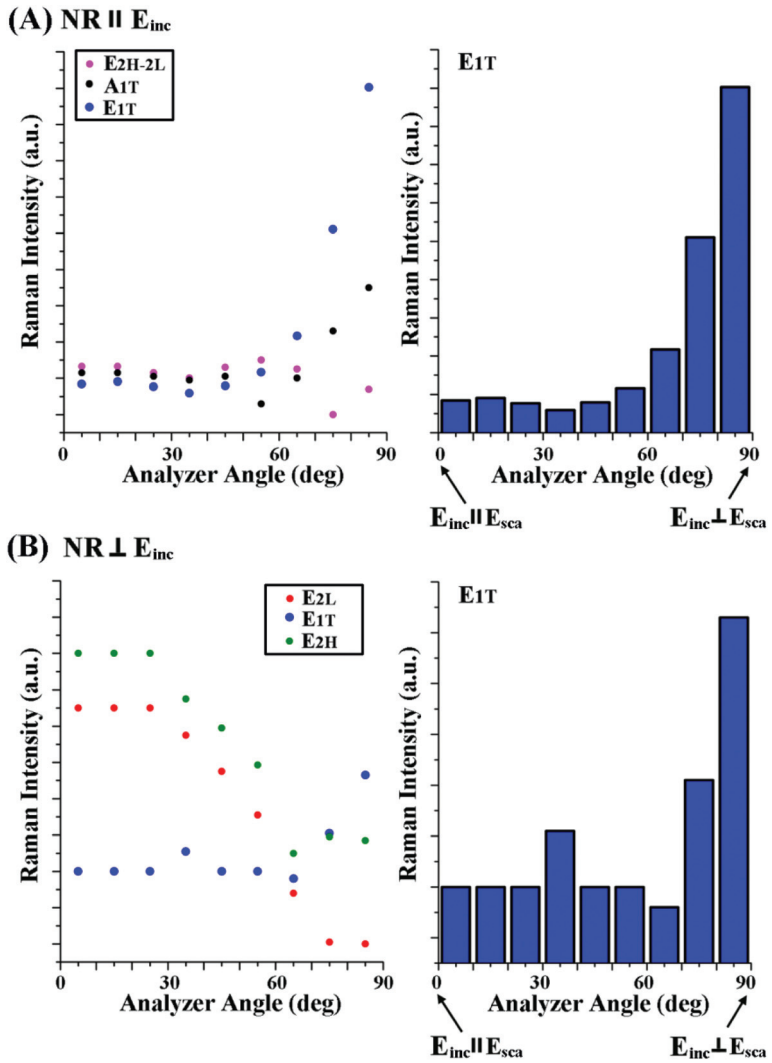

Fig. 5 The Raman scattering behaviors of the E_{1T} mode as well as the major modes for given light–matter interaction geometry were examined from the same ZnO NR while varying the analyzer rotation under the vertical and horizontal NR orientations. The linearly polarized laser was centered at the middle of the NR and the scattered Raman signals were probed in a cross polarized setting for different polarization states, ranging from 0° ($E_{inc}||E_{sca}$) to 90 deg ($E_{inc}\perp E_{sca}$). (A) Under NR$||E_{inc}$, the E_{1T} intensities became highly pronounced relative to the major peaks of $E_{2H}-E_{2L}$ and A_{1T} as the cross polarization condition was changed towards $E_{inc}\perp E_{sca}$. (B) The intensity of the E_{1T} mode also increased for the NR$\perp E_{inc}$ case when the $E_{inc}\perp E_{sca}$ setting was reached. The signals from the major peaks of E_{2L} and E_{2H} tended to decrease as E_{inc} became perpendicular to E_{sca}.

reported previously. Hence, our finding signifies that the Raman scattering behaviors from individual ZnO NRs become highly position-dependent when the forbidden modes of ZnO are evaluated, and should be interpreted accordingly as a function of the position along the NR.

From the electromagnetic enhancement point of view, a greater E_{inc} field can be assumed at the NR termini relative to the main body similar to the lightning rod effect seen in surface enhanced or tip enhanced Raman scattering.[44–46] More recently, similar Raman enhancement effects were reported for other systems beyond the commonly known, noble metals of Au and Ag. Metal oxide nanomaterials such as iron oxide and vanadium oxide were exploited in nonplasmon-based, Raman enhancement.[47,48] These studies also indicated that the metal oxide-based enhanced Raman scattering can be applicable to a variety of systems such as TiO_2, WO_3, and ZnO.[47,48] Hence, higher Raman scattering observed at the ZnO NR ends in this study could be considered to arise potentially from this enhanced E_{inc} field. Yet, this consideration cannot still account for the fact that not all Raman modes were equally affected under the same E_{inc} condition. In fact, a much more significant increase in Raman intensities were detected at the NR ends for the minor modes, but no distinct increase in scattering intensities were noted for the major phonon modes. And this trend persisted regardless of the light–matter interaction geometry. These results indicate that the origin of the unusual Raman behaviors associated with individual ZnO NRs lie elsewhere.

Although not specifically pertaining to Raman transitions, we have previously observed unusual optical phenomena simi-

larly occurring at the end positions of individual ZnO NRs. For example, the elastic scattering behaviors of single ZnO NRs under certain light–matter interaction geometry led to intense signals only at the two NR ends.[12–15,49] In another instance, fluorescence signals emitted from biomolecules such as proteins and DNA exhibited much greater intensities at the two ends of ZnO NRs relative to those from the NR main body.[1,18–20] Factors such as shape anisotropy, crystalline quality, and light–matter interaction orientation were crucial in controlling the NR position-dependent elastic scattering signals in the former case. For the latter, factors such as fluorophore spectroscopic characteristic, NR dimension, and shape anisotropy were important in enhancing the degree of fluorescence intensification at the NR ends whose process was based on the NR's subwavelength guiding and surface evanescent wave propagation of visible light. Specifically, the high shape anisotropy inherent to ZnO NRs played an important role in both circumstances.[13–15,19,20,50] We hypothesize that, similarly for Raman, the high shape anisotropy of 1D ZnO nanomaterials may cause the NR position-dependent abnormalities in Raman scattering.

To further evaluate this potential influence of the high shape anisotropy of the ZnO NRs, we performed control Raman measurements on isotropic ZnO MPs, exhibiting an average aspect ratio of approximately 1 : 1 (width : length). Fig. 6 shows the summary of the Raman data obtained from these control experiments. Upon synthesis, ZnO MPs are found to expose two different crystalline planes as shown in Fig. 1(C), the hexagonal basal plane and the rectangular prismic plane facing up. 40 and 24 ZnO MPs of random orientations, exposing their basal and prismic planes, respectively, were examined in the control experiments. We observed the same Raman intensity trend from the five peaks consistently on all ZnO MPs examined, showing the E_{2H} and E_{2L} modes as the predominant transitions regardless of the crystal planes, as shown in Fig. 6A. We then acquired position-resolved Raman spectra on the ZnO MPs. Fig. 6B shows subsequent Raman data taken from both the middle and edge areas of a single ZnO MP exposing its basal plane. From the intensity comparison between the five Raman modes, it is evident that there is no discernable difference in signals measured in the middle *versus* at the edge of the MP, both showing E_{2H} and E_{2L}

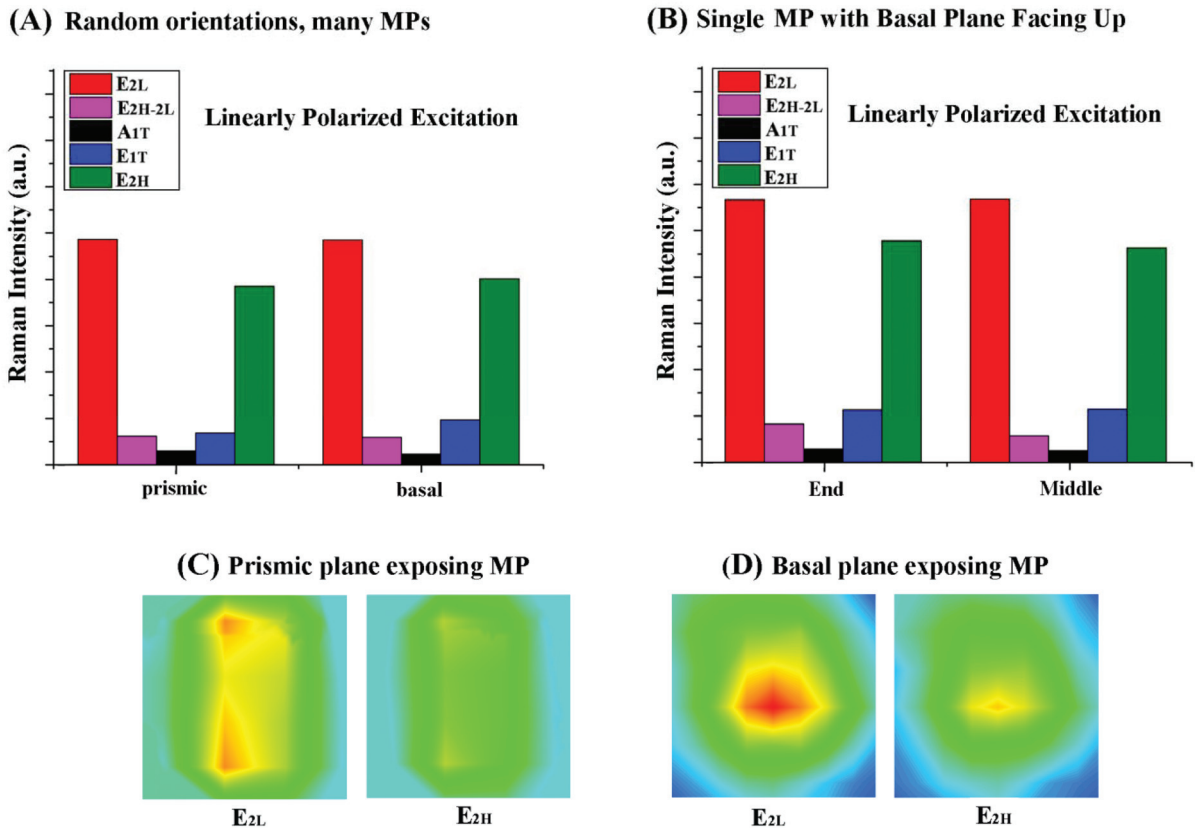

Fig. 6 Raman data collected from isotropic ZnO MPs are summarized. (A) The five phonon modes were compared for their intensities measured on the prismic *versus* basal facets of ZnO MPs using a linearly polarized incident light and no analyzer. Regardless of the crystalline facets and their orientations with respect to the incident polarization, the E_{2L} and E_{2H} modes exhibited dominant intensities. (B) The same trend in the Raman mode intensities were observed regardless of the different positions on each facet examined. In all cases, the strongest signals were produced by the E_{2L} and E_{2H} modes. (C and D) Raman intensity maps of the two dominant of E_{2L} and E_{2H} modes are displayed for a ZnO MP presenting a prismic facet in (C) and a basal facet in (D). In both panels, Raman signals were stronger at the center and weaker at the edge due to better overlap of the incident beam with the MP at the center which decreases as it moves towards the edge of the MP.

peaks as the dominant ones. In addition, Raman intensities from individual ZnO MPs were mapped by rastering the beam across the MPs. Fig. 6C and D display representative raster results for the dominant, E_{2H} and E_{2L}, Raman modes after mapping individual ZnO MPs exposing the prismic and basal plane, respectively. In both cases, Raman signals for the E_{2H} and E_{2L} modes were strongest in the middle of the MPs and their intensities decreased near the MP edges. The stronger intensity of the Raman signals at the center of the MPs is due to this position maximal overlap of the incident beam with the MP mass. As the incident beam was placed closer to the edges, Raman intensity gradually decreased since the effective illumination area on the ZnO MPs relative to the Si substrate reduced at the particle boundaries. Regardless, the mapped Raman data in Fig. 6C and D reveal that the position-dependent scattering effect tends to decrease as the ZnO becomes isotropic in shape. The scattering profiles from the isotropic MPs in Fig. 6 are contrary to the Raman scattering characteristics identified from the highly anisotropic ZnO NRs. As discussed earlier for the NRs, Raman signals were generally higher at the NR ends than the NR middle (*i.e.* main body). In particular, even forbidden modes could yield very intense, spatially confined scattering signals at the NR ends.

The ZnO NR and MP results combinedly demonstrate that the high shape anisotropy of the 1D nanomaterials plays a critical role in the unique, NR position-sensitive, Raman scattering characteristics of single ZnO NRs. The key significance of our study is that ZnO NR-position specific scattering behaviors were thoroughly examined for all five fingerprint Raman modes, which subsequently resulted in the identification of unique NR end behaviors depending on the light–matter interaction geometry. By validating with a large number of NRs, various NR positions, and five different phonon modes, our results systematically show that Raman behaviors of the NR ends are indeed drastically different than those of the NR main body. Hence, it is not always suitable to assume that the scattering intensities of allowed or forbidden modes are uniformly and equally present on all positions of highly isotropic nanomaterials such as ZnO NRs and, hence, any generalization of the Raman behaviors from NR position-averaged data should be done in caution. Our findings in this study may promote novel applications of polarized Raman scattering whose optical outputs can be selectively modulated along the various positions on individual ZnO NRs. The position-resolved understanding of the polarized Raman responses from individual ZnO NRs provided in this work may also facilitate the accurate correlation of Raman scattering data with the NR properties pertinent to their optical and optoelectronic applications.

Conclusion

We have elucidated polarization-controlled Raman scattering behaviors of wurtzite ZnO NRs and MPs by explicitly determining their spatially distinct scattering profiles from individual nanomaterials. We have examined the five fingerprint Raman modes of ZnO NRs (E_{2L}, E_{2H-2L}, A_{1T}, E_{1T}, E_{2H}) and identified polarization-specific, major and minor modes. We have subsequently ascertained polarization-specific behaviors of each phonon mode as a function of the position on the NR, consistent and incongruous with the Raman selection rules. In particular, we have reported a unique position-sensitive Raman scattering effect observed only from the NR ends which is related to the highly intense, NR end-localized scattering signals exhibited by the minor modes for given light–matter interaction geometry. By systematically comparing scattering features of individual ZnO NRs to the profiles of individual MPs, we have shown that the polarization- and position-dependent Raman characteristics of ZnO NRs are absent in Raman profiles from the isotropic MPs. Consequently, we confirmed that the very strong, NR end-localized Raman scattering from the minor modes in ZnO NRs originates from the large shape anisotropy inherent to the NRs.

Acknowledgements

The authors acknowledge financial support of this work by the ACS Petroleum Research Fund Award (55283-ND10) and the National Science Foundation Major Research Instrumentation Award (CHE1429079).

References

1 J. Hahm, *Annu. Rev. Phys. Chem.*, 2016, **67**, 691–717.
2 R. Yan, D. Gargas and P. Yang, *Nat. Photonics*, 2009, **3**, 569–576.
3 P. J. Pauzauskie and P. Yang, *Mater. Today*, 2006, **9**, 36–45.
4 Z. L. Wang, *ACS Nano*, 2008, **2**, 1987–1992.
5 Z. L. Wang, *J. Phys.: Condens. Matter*, 2004, **16**, R829–R858.
6 J. C. Johnson, H. Yan, H.-J. Choi, K. P. Knutsen, P. B. Petersen, M. Law, P. Yang and R. J. Saykally, *Proc. SPIE*, 2010, **5223**, 187–196.
7 D. J. Sirbuly, A. Tao, M. Law, R. Fan and P. Yang, *Adv. Mater.*, 2007, **19**, 61–66.
8 M. Law, D. J. Sirbuly, J. C. Johnson, J. Goldberger, R. J. Saykally and P. Yang, *Science*, 2004, **305**, 1269–1273.
9 D. J. Gargas, M. C. Moore, A. Ni, S.-W. Chang, Z. Zhang, S.-L. Chuang and P. Yang, *ACS Nano*, 2010, **4**, 3270–3276.
10 J. C. Johnson, H. Yan, R. D. Schaller, L. H. Haber, R. J. Saykally and P. Yang, *J. Phys. Chem. B*, 2001, **105**, 11387–11390.
11 M. H. Huang, S. Mao, H. Feick, H. Q. Yan, Y. Y. Wu, H. Kind, E. Weber, R. Russo and P. D. Yang, *Science*, 2001, **292**, 1897–1899.
12 D. S. Choi, D. Y. Joh, T. Lee, M. Milchak, H. Zhou, Y. Kang and J. Hahm, *Appl. Phys. Lett.*, 2014, **104**, 083112.
13 D. S. Choi, M. Singh, S. Song, J. Y. Chang, Y. Kang and J. Hahm, *Photonics*, 2015, **2**, 684.

14 D. S. Choi, M. Singh, H. Zhou, M. Milchak and J. Hahm, *Appl. Phys. Lett.*, 2015, **107**, 151110.
15 D. Choi, M. Singh, S. Song, J. Chang, Y. Kang and J. Hahm, *Photonics*, 2015, **2**, 684–701.
16 J. C. Johnson, H. Yan, P. Yang and R. J. Saykally, *J. Phys. Chem. B*, 2003, **107**, 8816–8828.
17 D. J. Sirbuly, M. Law, P. Pauzauskie, H. Yan, A. V. Maslov, K. Knutsen, C.-Z. Ning, R. J. Saykally and P. Yang, *Proc. Natl. Acad. Sci. U. S. A.*, 2005, **102**, 7800–7805.
18 M. Singh, A. Alabanza, L. E. Gonzalez, W. Wang, W. B. Reeves and J. Hahm, *Nanoscale*, 2016, **8**, 4613–4622.
19 M. Singh, S. Song and J. Hahm, *Nanoscale*, 2014, **6**, 308–315.
20 M. Singh, R. Jiang, H. Coia, D. S. Choi, A. Alabanza, J. Y. Chang, J. Wang and J. Hahm, *Nanoscale*, 2015, **7**, 1424–1436.
21 C. Zhang, F. Zhang, T. Xia, N. Kumar, J. Hahm, J. Liu, Z. L. Wang and J. Xu, *Opt. Express*, 2009, **17**, 7893–7900.
22 S. Chu, G. Wang, W. Zhou, Y. Lin, L. Chernyak, J. Zhao, J. Kong, L. Li, J. Ren and J. Liu, *Nat. Nanotechnol.*, 2011, **6**, 506–510.
23 R. Yan, J.-H. Park, Y. Choi, C.-J. Heo, S.-M. Yang, L. P. Lee and P. Yang, *Nat. Nanotechnol.*, 2012, **7**, 191–196.
24 F. Decremps, J. Pellicer-Porres, A. M. Saitta, J.-C. Chervin and A. Polian, *Phys. Rev. B: Condens. Matter*, 2002, **65**, 092101.
25 K. A. Alim, V. A. Fonoberov, M. Shamsa and A. A. Balandin, *J. Appl. Phys.*, 2005, **97**, 124313.
26 T. Gruber, G. M. Prinz, C. Kirchner, R. Kling, F. Reuss, W. Limmer and A. Waag, *J. Appl. Phys.*, 2004, **96**, 289–293.
27 G. W. Cong, H. Y. Wei, P. F. Zhang, W. Q. Peng, J. J. Wu, X. L. Liu, C. M. Jiao, W. G. Hu, Q. S. Zhu and Z. G. Wang, *Appl. Phys. Lett.*, 2005, **87**, 231903.
28 S. Singamaneni, M. Gupta, R. Yang, M. M. Tomczak, R. R. Naik, Z. L. Wang and V. V. Tsukruk, *ACS Nano*, 2009, **3**, 2593–2600.
29 R. Srikantharajah, K. Gerstner, S. Romeis and W. Peukert, *Nanoscale*, 2016, **8**, 7672–7682.
30 C.-T. Chien, M.-C. Wu, C.-W. Chen, H.-H. Yang, J.-J. Wu, W.-F. Su, C.-S. Lin and Y.-F. Chen, *Appl. Phys. Lett.*, 2008, **92**, 223102.
31 J. L. Yu, Y. F. Lai, Y. Z. Wang, S. Y. Cheng and Y. H. Chen, *J. Appl. Phys.*, 2014, **115**, 033505.
32 V. Adalsteinsson, O. Parajuli, S. Kepics, A. Gupta, W. B. Reeves and J. Hahm, *Anal. Chem.*, 2008, **80**, 6594–6601.
33 N. Kumar, A. Dorfman and J. Hahm, *J. Nanosci. Nanotechnol.*, 2005, **5**, 1915–1918.
34 A. Dorfman, N. Kumar and J. Hahm, *Adv. Mater.*, 2006, **18**, 2685–2690.
35 A. Dorfman, N. Kumar and J. Hahm, *Langmuir*, 2006, **22**, 4890–4895.
36 R. Cuscó, E. Alarcón-Lladó, J. Ibáñez, L. Artús, J. Jiménez, B. Wang and M. J. Callahan, *Phys. Rev. B: Condens. Matter*, 2007, **75**, 165202.
37 C. A. Arguello, D. L. Rousseau and S. P. S. Porto, *Phys. Rev.*, 1969, **181**, 1351–1363.
38 J. M. Calleja and M. Cardona, *Phys. Rev. B: Solid State*, 1977, **16**, 3753–3761.
39 D. Das and P. Mondal, *RSC Adv.*, 2014, **4**, 35735–35743.
40 D. N. Montenegro, V. Hortelano, O. Martínez, M. C. Martínez-Tomas, V. Sallet, V. Muñoz-Sanjosé and J. Jiménez, *J. Phys. D: Appl. Phys.*, 2013, **46**, 235302.
41 H. Hiroshi, *J. Phys.: Condens. Matter*, 2002, **14**, R967–R993.
42 J. Hahm, *J. Nanosci. Nanotechnol.*, 2014, **14**, 475–486.
43 J. Hahm, in *Metal-Enhanced Fluorescence*, ed. C. D. Geddes, John Wiley & Sons, Hoboken, NJ, 2010, ch. 12, pp. 363–391.
44 L. Meng, T. Huang, X. Wang, S. Chen, Z. Yang and B. Ren, *Opt. Express*, 2015, **23**, 13804–13813.
45 E. A. Pozzi, G. Goubert, N. Chiang, N. Jiang, C. T. Chapman, M. O. McAnally, A.-I. Henry, T. Seideman, G. C. Schatz, M. C. Hersam and R. P. V. Duyne, *Chem. Rev.*, 2017, **117**(7), 4961–4982.
46 P. F. Liao and A. Wokaun, *J. Chem. Phys.*, 1982, **76**, 751–752.
47 L. Li, T. Hutter, A. S. Finnemore, F. M. Huang, J. J. Baumberg, S. R. Elliott, U. Steiner and S. Mahajan, *Nano Lett.*, 2012, **12**, 4242–4246.
48 L. Li, U. Steiner and S. Mahajan, *Nano Lett.*, 2014, **14**, 495–498.
49 J. Truong, M. Singh, M. Hansen and J.-I. Hahm, *Nanoscale*, 2017, DOI: 10.1039/C7NR02201H.
50 M. Singh, X. Zhuo, D. S. Choi, L. E. Gonzalez, J. Wang and J. Hahm, *Nanoscale*, 2015, **7**, 18813–18826.